Nano Energy 32 (2017) 294–301

Contents lists available at ScienceDirect

Nano Energy

journal homepage: www.elsevier.com/locate/nanoen

Communication

Ti^{3+}-free three-phase $Li_4Ti_5O_{12}/TiO_2$ for high-rate lithium ion batteries: Capacity and conductivity enhancement by phase boundaries

Shitong Wang[a,b], Yong Yang[c], Wei Quan[a], Ye Hong[a], Zhongtai Zhang[a], Zilong Tang[a,*], Ju Li[b,d,**]

[a] State Key Lab of New Ceramics and Fine Processing, School of Materials Science and Engineering, Tsinghua University, Beijing 100084, PR China
[b] Department of Nuclear Science and Engineering, Massachusetts Institute of Technology, Cambridge, MA 02139, USA
[c] Department of Chemistry, Tsinghua University, Beijing 100084, PR China
[d] Department of Materials Science and Engineering, Massachusetts Institute of Technology, Cambridge, MA 02139, USA

ARTICLE INFO

Keywords:
$Li_4Ti_5O_{12}/TiO_2$
Phase boundaries
High-rate
Full pouch cell
Lithium ion battery

ABSTRACT

Ti-based nanoplates with abundant phase boundaries have been synthesized via partial lithiation reaction and optimized heat treatment. Using phase boundaries (rather than free surfaces) to keep the crystalline domains small might have significant advantages, such as improved tap density (therefore volumetric energy density) and reduced loss of live Lithium to the solid electrolyte interphase (SEI) which only coats the free surfaces. As lithium ion battery anode, the obtained $Li_4Ti_5O_{12}/TiO_2$(Anatase)/TiO_2(Rutile) three-phase mixture shows a capacity of about 170 mA h g^{-1} at 4000 mA g^{-1} (fully charged in ~150 s), and undergoes more than one thousand cycles with capacity fade of only 0.02% per cycle. It also demonstrates excellent cycling stability even after 4000 cycles at 500 mA g^{-1} in a Li-matched full cell vs. $LiFePO_4$ cathode in large pouch cell format, with tolerable gassing behavior. Rather than relying on Ti^{3+} defects or excessively large surface area, the present material is prepared in fully oxidizing environment, with abundant phase boundaries as the main capacity enhancement mechanism, which simplify its industrial production.

1. Introduction

Ti-based materials, such as Li-titanates and various TiO_2 polymorphs, have received considerable attention as LIB anode materials owing to their outstanding high-rate capacity and cycling stability, as well as their improved safety over graphite [1]. $Li_4Ti_5O_{12}$ (LTO) is considered to be one of the most promising anode materials due to its good structural stability with almost zero volume change despite lithium insertion/extraction. It features a flat discharge and charge plateau at 1.55 V vs Li/Li^+, which could avoid reductive decomposition of electrolyte and formation of lithium metal dendrites [2]. TiO_2 polymorphs, especially anatase TiO_2 (TiO_2-A), rutile TiO_2 (TiO_2-R) and TiO_2-B, also have an appropriate operating potential range (1.0–3.0 V vs. Li^+/Li) and excellent Li-ion insertion/extraction reversibility with low volume expansion (less than 4%) [3]. However, some aspects of Ti-based materials impede their applications, including their poor electronic conductivity and low lithium diffusion coefficient. Most commonly adopted solutions to these problems are based on doping or compositing with high electron/ion diffusion conductors in the bulk or surface [2,4,5].

Reducing particle size and introducing multi-phase compounds will increase interfacial areas, which can provide additional Li storage sites and improve electronic and ionic conductivities [6,7]. Some researchers have reported the synthesis of binary $Li_4Ti_5O_{12}/TiO_2$-A or $Li_4Ti_5O_{12}/TiO_2$-R composites by controlling the Li/Ti ratio [8–10], with mostly spherical morphology. On the other hand, two-dimensional (2D) layered nanomaterials might offer unique advantages in transport and strain accommodation [11,12]. Wu et al. has synthesized ultrathin anatase TiO_2/TiO_2-B nanosheets around the phase transition temperature and the capacity was enhanced by phase boundaries [6]. According to the Gibbs phase rule, it is possible to obtain three-phase co-existence, e.g. $Li_4Ti_5O_{12}/TiO_2$-A/TiO_2-R, if we tune the temperature and Li/Ti ratio together, which should give more phase boundaries. Using phase boundaries (rather than free surfaces) to keep the crystalline domains small might have significant advantages, such as improved tap density (therefore volumetric energy density) and reduced loss of live Lithium to the solid electrolyte interphase (SEI) which only coats the free surfaces. To our knowledge, this approach of utilizing three-phase equilibrium and 2D nanoarchitecture to enhance electrochemical performance was not reported before.

* Corresponding author at: School of Materials Science and Engineering, Tsinghua University, Beijing 100084, PR China.
** Corresponding author at: Department of Nuclear Science and Engineering and Department of Materials Science and Engineering, Massachusetts Institute of Technology, Cambridge, MA 02139, USA.
E-mail addresses: tzl@tsinghua.edu.cn (Z. Tang), liju@mit.edu (J. Li).

http://dx.doi.org/10.1016/j.nanoen.2016.12.052
Received 22 October 2016; Received in revised form 14 December 2016; Accepted 26 December 2016
Available online 27 December 2016

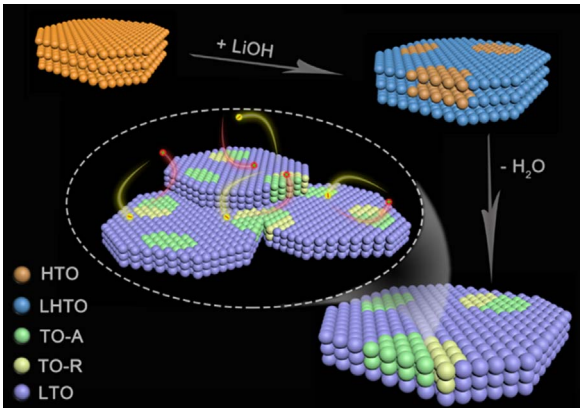

Fig. 1. Schematics of the synthesis procedure. The insert in the white circle shows the fast lithium insertion/extraction within the material.

In this paper, $Li_4Ti_5O_{12}/TiO_2$-A/TiO_2-R (abbreviated as LTO/A/R) three-phase nanoplates with abundant phase boundaries have been obtained via partial lithiation and optimized heat treatment. $Li_{1.81}H_{0.19}Ti_2O_5{\cdot}xH_2O$ (LHTO) nanosheets with $H_2Ti_2O_5{\cdot}xH_2O$ (HTO) domains were designed as the precursors via incomplete lithiation of protonated titanate (see the schematic in Fig. 1). During the subsequent dehydration process, $Li_4Ti_5O_{12}$ and TiO_2-A grains grew from LHTO and HTO nanodomains, respectively, which preserved the rich-boundary and 2D nature of the precursor structure. Besides, the uniformly distributed nanocrystallites of LHTO and HTO precursors can be beneficial in restricting the growth as well as preventing the aggregation of $Li_4Ti_5O_{12}$ and TiO_2 nanograins. Thereafter, at the anatase→rutile phase transition temperature, TiO_2-A can partially change to TiO_2-R which can further increase phase boundary density. The resultant triple-phase $Li_4Ti_5O_{12}/TiO_2$-A/TiO_2-R nanoplates exhibited enhanced rate performance compared with previously reported Ti-based anode materials (including those modified with carbon), and still shows a capacity of about 139 mA h g^{-1} after 1000 cycles when fully charged at high current density of 4000 mA g^{-1}. In a Li-matched $LiFePO_4$ vs. $Li_4Ti_5O_{12}/TiO_2$ full cell battery (large-format pouch cell), the as-obtained electrode also manifests stable cycling for 4000 cycles at 500 mA g^{-1}, making it a promising material for applications in quick-charging consumer electronics, electric vehicles and stationary energy storage.

2. Experimental section

2.1. Materials synthesis

The preparation of lithium titanate hydrates consists of three steps. First, layered protonated titanate was prepared via hydrothermal reaction between anatase TiO_2 powders and concentrated NaOH solution at 150 °C for several hours, following the ion substitution progress of Na^+ with H^+ in 0.5 M HNO_3 solution. Second, layered LHTO/HTO precursor was obtained by chemical lithiation of hydrogen trititanate in a 0.8 M LiOH solution heated at 120 °C for 12 h in a Teflon-lined stainless steel autoclave. Lastly, LTO/A/R and LTO/A were synthesized by heating in air for 3 h at 500 °C and 400 °C, respectively. For the preparation of LTO for benchmark purposes, the LHTO precursor was obtained by complete chemical lithiation of hydrogen trititanate in an excessive LiOH solution with the same concentration (0.8 M). And then, LTO sample was calcined at the same heat treatment condition of LTO/A/R.

2.2. Materials characterization

Powder X-ray diffraction (XRD) was recorded on a Bruker D8 Advance with Cu Kα radiation (λ=1.5418 Å). Thermogravimetric and differential scanning calorimetry (TG-DSC) analysis was carried out using NETZSCH-STA 449 F3 with a heating rate of 2 °C min^{-1} in air. Inductively coupled plasma mass spectroscopy (ICP-MS) analysis was carried out using iCP QC (Thermo Fisher Scientific, US) for lithium and titanium content. Nitrogen adsorption–desorption isotherms were obtained using an Automated vapor sorption analyzer (Autosorb-iQ2-MP (Quanta Chrome)) at 77.4 K under vacuum. The specific surface area was calculated by the Brunauer-Emmett-Teller (BET) method. The morphology, size and crystal structure of the as-prepared samples were characterized by MERLIN VP Compact for scanning electron microscope (SEM), Hitachi-HT7700 for transmission emission microscopy (TEM), JEM-2100F for high resolution transmission electron microscopy (HRTEM) and selected-area electron diffraction (SAED).

2.3. Electrochemical measurements

The electrochemical measurements were conducted by using 2032-coin half cells and full batteries in large pouch cell format. The working electrode consisted of active material, Super P and binder (polyvinylidene fluoride) in a weight ratio of 80:10:10 in *N*-methyl-2-pyrrolidene (NMP) solution. The obtained slurry was coated onto 16 μm thickness Al foil via scraper machine and dried at 120 °C in a vacuum oven for 12 h. Roll squeezer was used to enhance the contact between material and foil, together with increasing the compaction density (resulting in the porosity of electrodes less than 50%). The 2032-coin-type cells were assembled in an argon-filled glove-box using pure lithium foil as both the counter electrode and reference electrode, and a microporous membrane (Celguard 2400, USA) as a separator. 80 μL of 1.0 M $LiPF_6$ in a mixture (1:1 vol ratio) of ethylene carbonate (EC) and dimethylcarbonate (DMC) was added as the electrolyte. The mass loading of the anode (12 mm diameter) in this work is ~1.0 mg cm^{-2}. IM6 (Bas-Zahner, Germany) electrochemical workstation was used for cyclic voltammetry (CV) with the scan scope of 1.0–2.5 V and also for electrochemical impedance spectroscopy (EIS) from 100 kHz to 10 MHz, with a perturbation of 5 mV applied. For pouch-cell batteries, $LiFePO_4$ vs. LTO/A/R with a capacity of 30 mAh were assembled using the same electrodes, electrolyte, and separator as the half cells. Both the substrates of $LiFePO_4$ cathode and LTO/A/R anode are Al foils. The $LiFePO_4$ cathode has 30% excess capacity compared to the anode. All the cells were conducted on a battery test (LAND 2001 A Cell test system) and cycled between 1.0–2.5 V (half cells) and 1.2–2.4 V (full cells) at room temperature.

3. Results

3.1. Synthesis and characterization

We set out with layered protonated titanate with a formula of $H_2Ti_nO_{2n+1}{\cdot}H_2O$, such as $H_2Ti_2O_5{\cdot}H_2O$ and $H_2Ti_3O_7$, which are well known to form nanotubes and nanosheets [5]. 2D $Li_{1.81}H_{0.19}Ti_2O_5{\cdot}xH_2O$ precursor is usually prepared by hydrothermal lithiation of layered protonated titanate in lithium hydroxide solution [13]. In this work, we first reported the synthesis of a dual-phase $Li_{1.81}H_{0.19}Ti_2O_5{\cdot}xH_2O$ and $H_2Ti_2O_5{\cdot}xH_2O$ precursor (hereinafter referred to LHTO and HTO, respectively) via incomplete lithiation of protonated titanate. Inductively coupled plasma emission spectroscopy (ICP) revealed the Li/Ti mole ratio of LHTO/HTO precursor to be 0.71, which means HTO would not be fully converted to LHTO due to the lack of LiOH. Owing to the advantage of homogeneous reaction between solid and fluid for hydrothermal processing [14], residual HTO domains can be uniformly distributed with LHTO domains on the nanosheets at nanoscale (Figs. S1 and S2), which is key for creating abundant interfaces in the dehydration process afterwards. Due to the low crystallinity and relatively small amount of protonated titanate in the precursor, HTO phase in the LHTO/HTO precursor is not apparent based on the XRD pattern (Fig. 2a). That is why most of the broad

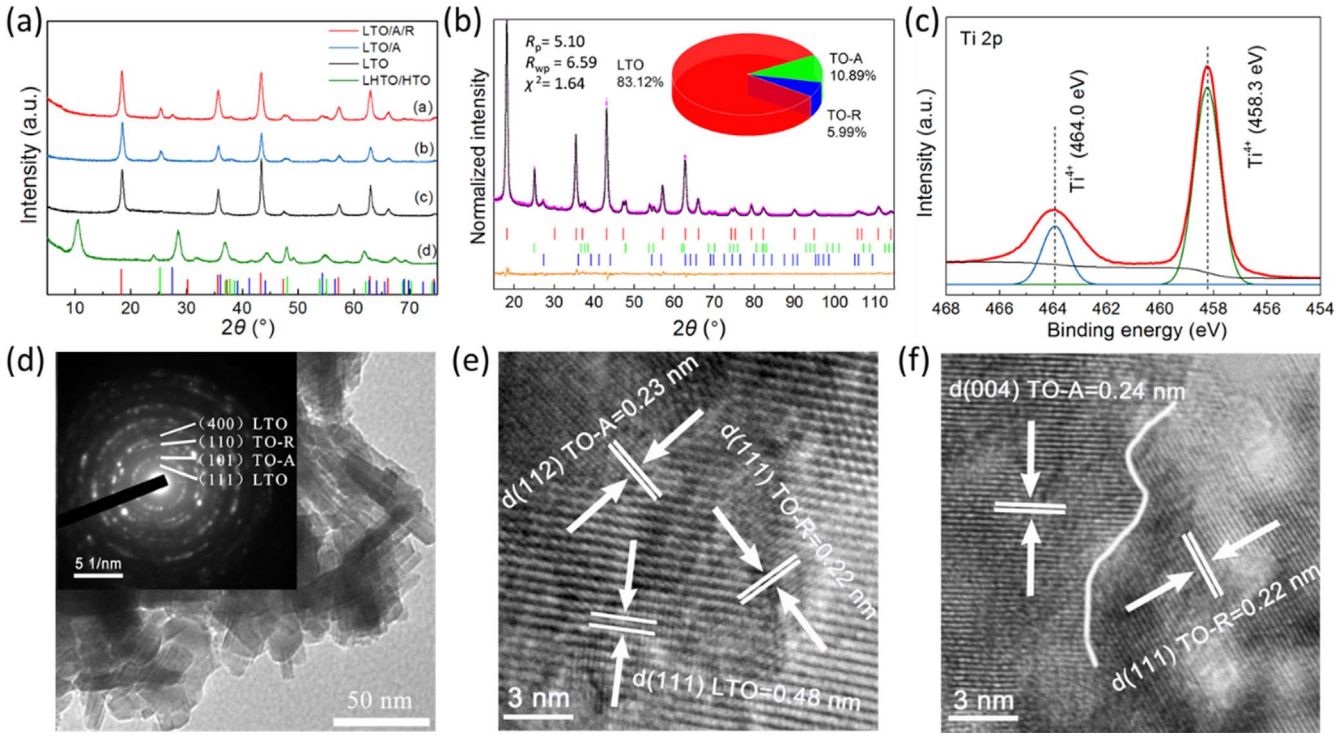

Fig. 2. (a) XRD patterns of LTO/A/R, LTO/A, LTO and LHTO/HTO with $Li_4Ti_5O_{12}$ (JCPDS No. 49-0207, red), anatase TiO_2 (JCPDS No. 89-4921, green) and rutile TiO_2 (JCPDS No. 21-1276, blue). (b) Rietveld refinement analysis for XRD patterns of LTO/A/R (purple: observed intensities; black: calculated intensities; orange: difference plot; red, green and blue makers indicate the position of the $Li_4Ti_5O_{12}$, TiO_2-A and TiO_2-R diffraction lines). (c) Ti 2*p* XPS spectra of LTO/A/R (red: observed data; black: background; blue and green: fitting data). (d) TEM and (e)-(f) HRTEM images of LTO/A/R. The insert in (d) SAED pattern of LTO/A/R.

peaks are consistent with $Li_{1.81}H_{0.19}Ti_2O_5{\cdot}xH_2O$ (JCPDS No. 47-0123). TG-DSC analysis (Fig. S3) of LHTO/HTO precursor revealed that the dehydration process came to an end above 500 °C, with only one tiny and broad peak around 510 °C associated with phase transition from TiO_2-A to TiO_2-R. According to the analysis above, 500 °C might be an optimal temperature to create $Li_4Ti_5O_{12}$/TiO_2-A/TiO_2-R three-phase materials (hereinafter referred to LTO/A/R) with abundant phase boundaries, at the same time, the 2D nanoarchitecture of LHTO/HTO precursor can also be inherited. The XRD pattern of the as-prepared LTO/A/R sample (Fig. 2a) shows the diffraction peaks consistent with spinel $Li_4Ti_5O_{12}$ (JCPDS No. 49-0207) and anatase TiO_2 (JCPDS No. 89-4921) and rutile TiO_2 (JCPDS No. 21-1276) with the individual sets of planes indexed respectively. To quantify the amount of these phase components, Rietveld refinement was conducted (Fig. 2b). The results showed the mass contents for $Li_4Ti_5O_{12}$, TiO_2-A and TiO_2-R are 83%, 11% and 6%, respectively.

Field emission scanning election microscopy (FESEM) and TEM characterize the morphology of LTO/A/R nanoplates (Figs. S4 and 2d, respectively), and the thickness of the nanosheets is about 5–10 nm. In selected area electron diffraction pattern (SAED), the material is represented by some rings corresponding to (111) and (400) planes of $Li_4Ti_5O_{12}$, (101) planes of TiO_2-A and (110) planes of TiO_2-R. Just as shown in the schematic Fig. 1, $Li_4Ti_5O_{12}$ and TiO_2 crystallites about several nanometers in size were dispersed on nanosheets (high resolution transmission electron microscopy image (HRTEM, Fig. S5)). Lattice fringes of TiO_2-A (112) plane and TiO_2-R (111) plane with a 90° angle are clearly observed (Fig. 2e). The interfaces and the lattice mismatch (*m*) can be calculated to be 4.44% using the following Eq. (1):

$$m = \frac{|d_1 \sin\theta - d_2|}{0.5 \times (d_1 \sin\theta + d_2)} \quad (1)$$

Similarly, lattice fringes of TiO_2-A (004) plane and TiO_2-R (111) plane with a 60° angle (Fig. 2f) are also discovered, with *m* of 16.84%. It is worth mentioning that a large amount of obvious lattice distortion and disorder at the interface among $Li_4Ti_5O_{12}$/TiO_2-A/TiO_2-R are observed, which may provide more active sites for Li storage and more crystal defects for conductivity improvement [6,7].

For comparison, two other materials were synthesized. One is $Li_4Ti_5O_{12}$/TiO_2-A obtained from 400 °C heat treatment using the same LHTO/HTO precursor as LTO/A/R (hereinafter referred to LTO/A). All the diffraction peaks for LTO/A can be assigned to $Li_4Ti_5O_{12}$ and TiO_2-A (Fig. 2a), which suggests the transformation from TiO_2-A to TiO_2-R has not begun. The other is pure $Li_4Ti_5O_{12}$ (hereinafter referred to LTO) with less phase boundaries, which can be confirmed by TEM (Fig. S6). We choose $Li_{1.81}H_{0.19}Ti_2O_5{\cdot}xH_2O$ (LHTO) obtained from complete lithiation of protonated titanate as precursor. All the diffraction peaks for LTO can be assigned to $Li_4Ti_5O_{12}$ (Fig. 2a). Based on the Brunauer-Emmett-Teller (BET) measurement (Fig. S7), LTO, LTO/A and LTO/A/R sample has a specific surface area of 52 $m^2\,g^{-1}$, 71 $m^2\,g^{-1}$ and 64 $m^2\,g^{-1}$, respectively. The specific surface area of LTO/A higher than that of LTO/A/R, due to the coarser nanostructure of LTO/A/R obtained at higher temperature. As the heating process was conducted in air, Ti 2*p* X-ray photoelectron spectroscopy (XPS, Fig. 2c) spectra shows similar features of Ti^{4+} ions due to the Ti $2p_{3/2}$ (≈458.3 eV), Ti $2p_{1/2}$ (≈464.0 eV) [15], and no Ti^{3+} signal was detected. The capacity enhancement mechanism in this work is thus quite different from many Ti^{3+} defects enhanced Ti-based materials obtained in inert or reducing atmosphere [15,16], which can greatly simplify the heat treatment and save cost for practical production.

3.2. Electrochemical performance

Fig. 3a shows the first five CV scan curves of LTO/A/R with a scan rate of 0.1 mV s^{-1}. The main redox peaks at about 1.73/1.44 V and two minor peaks at 2.0 V/1.7 V correspond to the diffusion-controlled processes in $Li_4Ti_5O_{12}$ phase and TiO_2 phase, respectively. After the second cycle, both the peak position and curve shape of the following cycles are almost unchanged, which indicates a good stability of the

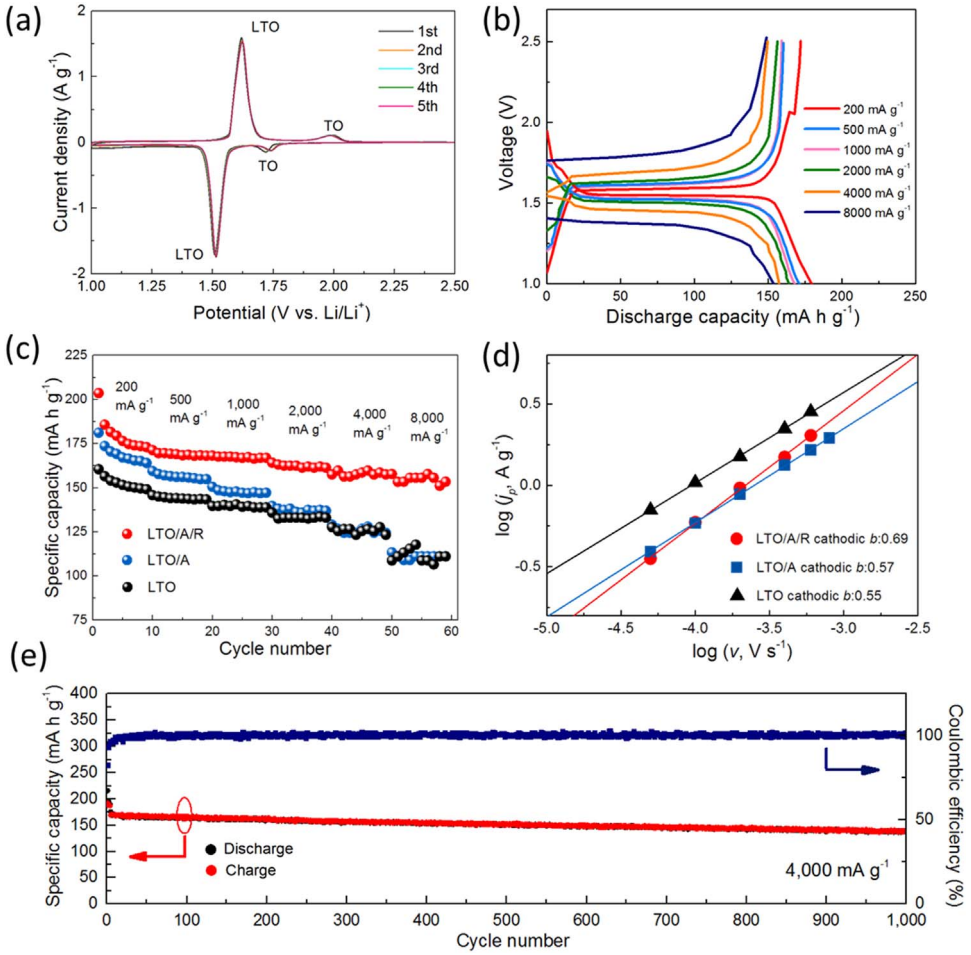

Fig. 3. Electrochemical performances of LTO/A/R, LTO/A and LTO samples. (a) CV of LTO/A/R in the first five cycles at scanning rate of 0.1 mV s^{-1}. (b) The charge-discharge voltage profiles of LTO/A/R at different current densities. Comparison among LTO/A/R, LTO/A and LTO samples for (c) rate capabilities at current densities from 200 to 8000 mA g^{-1} and (d) *b*-value determination of the peak cathodic current density from 0.05 mV s^{-1} up to 0.6 mV s^{-1}. (e) Graph of cycling stability and Coulombic efficiency of LTO/A/R at 4000 mA g^{-1}.

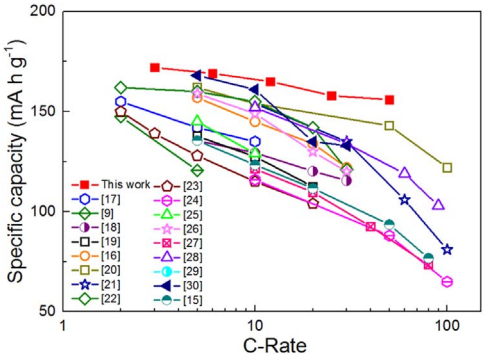

Fig. 4. Comparison of the rate performances of the as-prepared LTO/A/R with previously reported Ti-based anode materials. The details are listed in Table S1.

electrode reaction. The first five CV scan curves of LTO/A under the same condition were exhibited in Fig. S8. On one hand, the peaks of $Li_4Ti_5O_{12}$ phase in LTO/A/R are sharper than LTO/A, which is due to the higher crystallinity and coarser nanostructure of LTO/A/R obtained at higher temperature. On the other hand, the peaks of TiO_2 phase in LTO/A/R are broader and more flat than LTO/A, which might be caused by the reduced particle size of TiO_2-A and TiO_2-R as well as the increased phase boundaries between them. Fig. 3b shows the steady discharge/charge profiles of LTO/A/R anodes at various current densities of 200, 500, 1000, 2000, 4000 and 8000 mA g^{-1} in the voltage range of 1.0–2.5 V. At a relative low current density (200 mA g^{-1}), the electrode delivers a stable specific capacity as high as 179.5 mA h g^{-1}. As the current increased from 500 to 4000 mA g^{-1}, the specific capacities only slightly decreased from 171.3 to 168.2, 164.2 and 157.5 mA h g^{-1}, respectively. Even at very high current density of 8000 mA g^{-1}, the specific capacities remain as high as 155.6 mA h g^{-1}, corresponding to 86.7% of that at 200 mA g^{-1}. For comparison, when the current density increases from 200 to 1000 mA g^{-1}, the rate capabilities of LTO/A and LTO electrodes drop quickly from 165.4 to 147.2 mA g^{-1} and from 151.6 to 139.2 mA g^{-1}, respectively. At higher current density, the capacities of LTO/A and LTO tend to be similar, which are about 79% (at 4000 mA g^{-1}) and 71% (at 8000 mA g^{-1}) of those for LTO/A/R (Fig. 3c). The results indicate that the decrease of interfaces is detrimental to the rate and cycling performance. Furthermore, we compared LTO/A/R electrode with other Ti-based materials (including $Li_4Ti_5O_{12}$, various TiO_2 polymorphs and their composites) reported recently (see the comparison in Fig. 4 and Table S1) [9,15–30]. It manifests better rate capacity than the other electrodes (even including those modified by carbon), which suggests superior fast transport capability of lithium ion and electron during charging/discharging.

A plot of log(*i*) versus log(*v*) from 0.05 to 0.6 mV s^{-1} for the cathodic peaks (Fig. 3d) was presented assuming that the current obeys a power-law relationship with the sweep rate (Fig. S12) [31,32]:

$$i = av^b \quad (2)$$

where *a* and *b* are adjustable parameters and the value of *b* provides insight into the charge storage mechanism. For LTO/A and LTO

electrodes, *b*-values are 0.57 and 0.55, respectively, which are close to 0.5, indicating that the kinetics are mainly diffusion-controlled. LTO/A/R, as surface-controlled redox reaction caused by small particle size and interfacial storage in $Li_4Ti_5O_{12}$/TiO_2-A/TiO_2-R three-phase, presents *b*-value of 0.69, and leads to exceedingly excellent high-rate capacity. The low frequency Warburg contribution of the impedance response has been used to determine the Li-ion diffusivity (D_{Li}) at various charge of state (SOC) in the electrodes (Fig. 5a–c). The expression for D_{Li} can be written as [33–35]:

$$D_{Li}=\frac{1}{2}\left[\left(\frac{V_m}{FA\sigma_w}\right)\frac{dE}{dx}\right]^2 \quad (3)$$

where V_m is the molar volume (we defined V_m as 45.73 $cm^3\ mol^{-1}$ ($Li_4Ti_5O_{12}$) for simplification), F is the Faraday constant, A is the total contact area between the electrolyte and the electrode, and σ_w is the Warburg coefficient which was obtained from the Warburg region of impedance response. The σ_w values at different discharge depths (different potentials) can be obtained from the slope of lines in Z' vs. $\omega^{-1/2}$ plots (ω is the angular frequency) for the Warburg region (Fig. S13). The Z' vs. $\omega^{-1/2}$ plot for the low frequency Warburg region can be summarized as:

$$Z' = R+\sigma_w\omega^{-1/2} \quad (4)$$

The *dE/dx* obtained from discharge curve illustrates that the slopes of the discharge curve at 25%, 50%, 75% and 100% respectively (Fig. 5d–f). The Li-ion diffusivity (D_{Li}) of the three electrodes at different discharge depths are shown in Table 1. It should be noted that the Li-ion diffusivity of LTO/A/R (4.39×10^{-11}–3.48×10^{-8} $cm^2\ s^{-1}$) is about 1 order of magnitude higher than that of LTO. Although the LTO/A has higher specific surface area and less damaged 2D nanostructure, the Li-ion diffusivity is comparable to that of LTO/A/R. This demonstrates again the conductivity enhancement by abundant phase boundaries. As a result, the LTO/A/R electrode exhibits superior cycling capacity of about 170 mA h g^{-1} at a high current rate of 4000 mA g^{-1} (fully charged within ~150 s) and sustains more than one thousand cycles with a capacity fading rate of only 0.02% per cycle

Table 1
Li-ion diffusivity in LTO/A/R, LTO/A and LTO electrodes. The depths of discharge were marked in Fig. 5d–f.

Diffusivity Depth of discharge	LTO/A/R ($cm^2\ s^{-1}$)	LTO/A ($cm^2\ s^{-1}$)	LTO ($cm^2\ s^{-1}$)
25%	1.49×10^{-10}	2.73×10^{-10}	7.59×10^{-13}
50%	4.39×10^{-11}	1.28×10^{-10}	7.57×10^{-12}
75%	6.15×10^{-11}	4.26×10^{-11}	5.32×10^{-11}
100%	3.48×10^{-8}	1.31×10^{-9}	1.04×10^{-9}

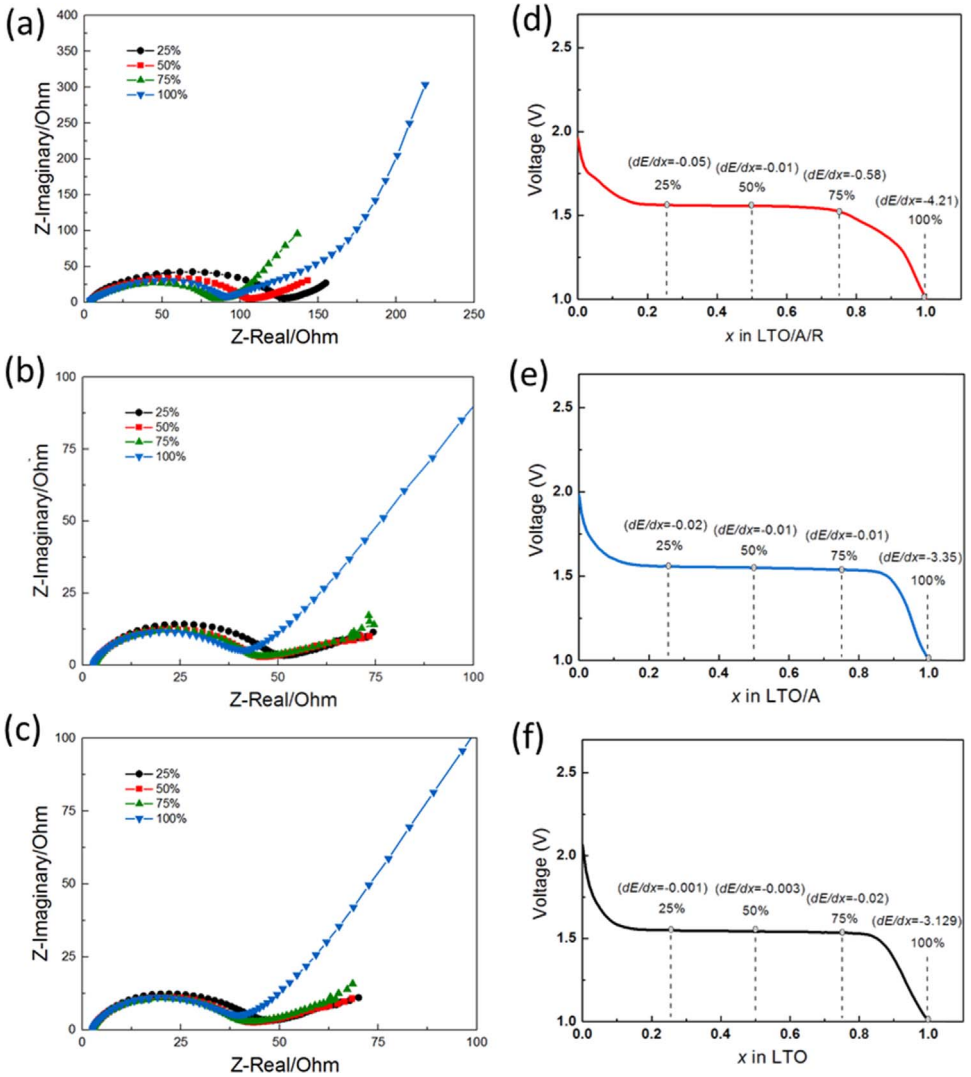

Fig. 5. EIS analysis of (a) LTO/A/R, (b) LTO/A and (c) LTO electrodes measured at different depths of discharge. Discharge curve at a current density of 50 mA g^{-1} of (d) LTO/A/R, (e) LTO/A and (f) LTO electrodes.

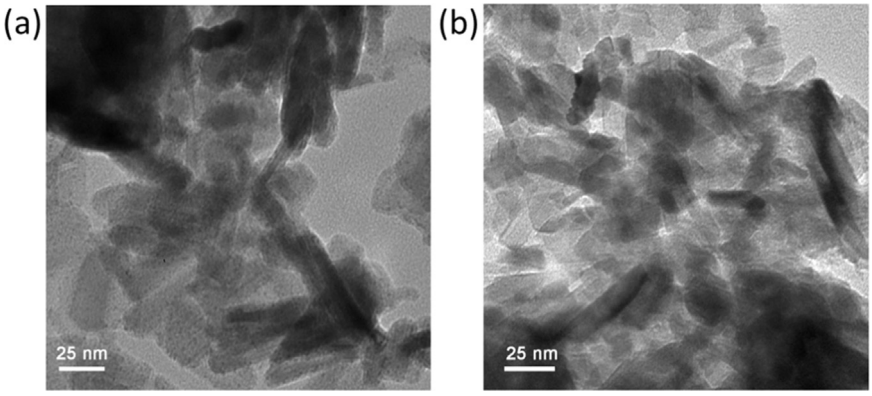

Fig. 6. TEM images of LTO/A/R (a) before and (b) after 1000 cycles.

(Fig. 3e). Moreover, nearly intact nanoplate morphology after 1000 ultrafast cycling of LTO/A/R was observed via TEM (Fig. 6), proving its outstanding accommodation of ultrafast lithium ions insertion/ extraction in LIBs.

4. Discussion

The "Coulombic inefficiency" (CI) is a measure of solid electrolyte interphase (SEI) stability for use in full cell batteries. CI is defined as ≡ 1 – Coulombic efficiency (CE), and is plotted on logarithmic scale (if CI is positive, it will be plotted in red; if CI is negative, |CI| will be plotted in green). In battery industry, if the CI of one electrode in half cell can get stably within $< 10^{-3}$ in the first 10 cycles, it is more possible for it to be used in full batteries because the formation of stable SEI does not consume too much "live" lithium ions. Fig. 7a illustrates calculated CI for LTO/A/R electrode at 4000 mA g^{-1}. The CI value for the first cycle is 10^{-1}, and then it dropped to ~10^{-3} after 7th cycle, followed by fluctuating values distributed between 10^{-2} and 10^{-4} for the following thousand cycles. We note that after the 7th cycle, there are more number of negative (green) CIs than positive (red) CIs, which means if a running-window average is done, the average CE actually exceeds 1 by a little. This may be explained by the reversible shuttling of soluble redox mediators in the electrolyte [36]. This result illustrated LTO/A/R electrode could posses excellent SEI stability and highly reversible Li-ion insertion/extraction properties, because if the SEI were to fall off / regrow repeatedly with cycling, the average CE should be less than 1 (average CI should be positive). To further verify this, we assembled $LiFePO_4$ cathode vs. LTO/A/R anode in soft package batteries and test their performances. The full battery delivered specific capacity of 128.1, 127.2, 126 and 118.6 mA h g^{-1} in the 2nd, 5th, 10th and 100th cycles. After 1000th cycles, only 17% of the initial capacity is lost in this lithium-matched full cell and the (dis)charge polarization did not increase during cycling (Fig. 7b). It also exhibits stable cycling capability above 85 mA h g^{-1} even after 4000 cycles at 500 mA g^{-1}. In addition, even though Ti ion is known to catalyze electrolyte decomposition, the gassing problem is not excessive and seen to be totally manageable after 4000 cycles in this large-format pouch full cell (Fig. 7c). This is due to the stable and inert SEI film (Fig. 6b) formed around the three-phase electrode in the first few charge/discharge cycles, which suppresses the Ti-catalyzed decomposition of electrolyte. From XPS, we know that Li_2CO_3 and ROCOOLi species were formed on the surface of the LTO/A/R electrodes (Fig. S14), due to the interfacial reactions between the LTO/A/R and electrolyte solution in the first few charge/discharge cycles, but making no influence on their performance

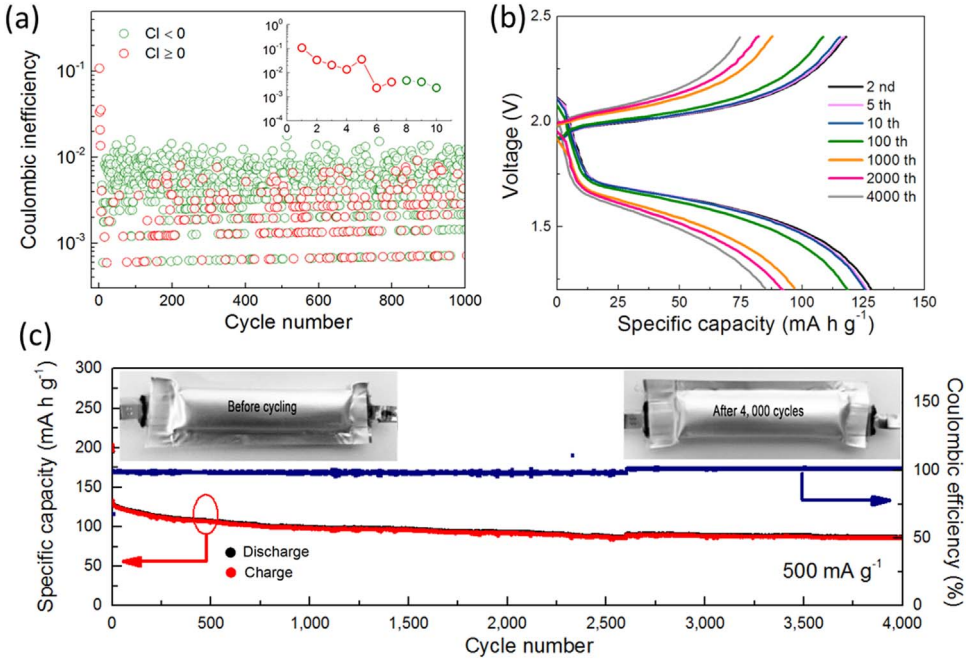

Fig. 7. (a) Coulombic inefficiency of LTO/A/R at 4000 mA g^{-1}, the insert magnifies CI for the first 10 cycles. (b) The charge-discharge voltage profiles at different cycles and (c) Cycling stability and Coulombic efficiency at 500 mA g^{-1} for $LiFePO_4$ vs. LTO/A/R full batteries. The inserts in (c) show the photographs of full batteries (left) before and (right) after 4000 cycles.

[26,37]. The outstanding electrochemical performance reveals the as-prepared $Li_4Ti_5O_{12}/TiO_2$ nanoplate to be a promising anode for real applications in fast-charging electronics and electric vehicles.

5. Conclusions

We successfully synthesized 2D $Li_4Ti_5O_{12}$/anatase TiO_2/rutile TiO_2 nanocomposites with plentiful phase boundaries via incomplete lithiation reaction and optimized heat treatment. The multiple boundaries on the nanoplates exhibited obvious advantages in enhancing capacity and conductivity. We implemented two simple approaches in obtaining Ti-based nanocomposites with a large amount of interfaces without coarsening: (i) to create layered LHTO/HTO precursors via partial lithiation of protonated titanate; (ii) to create abundant interfaces around the phase transition point, but trying to maintain the 2D morphology of precursors. Through this materials design, the obtained materials exhibited superior power rate and long cycle life for half coin cells as well as soft package full batteries. Furthermore, one can draw a conclusion that Ti^{3+} defects and carbon coating may not be the only approaches for the conductivity enhancement. Therefore one can produce Ti-based electrode materials with superior electrochemical performances in air instead of in inert or reducing atmosphere, which would simplify the heat treatment and save cost in industrial production. This three-phase, 2D composite designed strategy could be useful for other oxide electrodes in energy storage and conversion applications as well.

Acknowledgments

We would like to thank the gracious help of C. Settens at MIT for the Rietveld refinement analysis. Z.L.T. acknowledges support by the National Natural Science Foundation of China (no. 51472137). J.L. acknowledges support by NSF.ECCS-1610806.

Appendix A. Supplementary material

Supplementary data associated with this article can be found in the online version at http://dx.doi.org/10.1016/j.nanoen.2016.12.052.

References

[1] Z. Chen, I. Belharouak, Y.K. Sun, K. Amine, Adv. Funct. Mater. 23 (2013) 959–969.
[2] G.N. Zhu, Y.G. Wang, Y.Y. Xia, Energy Environ. Sci. 5 (2012) 6652–6667.
[3] C.H. Jiang, J.S. Zhang, J. Mater. Sci. Technol. 29 (2013) 97–122.
[4] Z.G. Yang, D. Choi, S. Kerisit, K.M. Rosso, D.H. Wang, J. Zhang, G. Graff, J. Liu, J. Power Sources 192 (2009) 588–598.
[5] Z.S. Hong, M.D. Wei, J. Mater. Chem. A 1 (2013) 4403–4414.
[6] Q. Wu, J. Xu, X. Yang, F. Lu, S. He, J. Yang, H.J. Fan, M. Wu, Adv. Energy Mater. 5 (2014) 1401756.
[7] A. Magasinski, P. Dixon, B. Hertzberg, A. Kvit, J. Ayala, G. Yushin, Nat. Mater. 9 (2010) 353–358.
[8] M.M. Rahman, J.Z. Wang, M.F. Hassan, D. Wexler, H.K. Liu, Adv. Energy Mater. 1 (2011) 212–220.
[9] L. Gao, R. Liu, H. Hu, G. Li, Y. Yu, Nanotechnology 25 (2014) 175402.
[10] Y.Q. Wang, L. Guo, Y.G. Guo, H. Li, X.Q. He, S. Tsukimoto, Y. Ikuhara, L.J. Wan, J. Am. Chem. Soc. 134 (2012) 7874–7879.
[11] J.H. Liu, X.W. Liu, Adv. Mater. 24 (2012) 4097–4111.
[12] V. Augustyn, J. Come, M.A. Lowe, J.W. Kim, P. Taberna, S.H. Tolbert, H.D. Abruña, P. Simon, B. Dunn, Nat. Mater. 12 (2013) 518–522.
[13] J.R. Li, Z.L. Tang, Z.T. Zhang, Electrochem. Commun. 7 (2005) 62–67.
[14] M. Yoshimura, K. Byrappa, J. Mater. Sci. 43 (2008) 2085–2103.
[15] J. Chen, W. Song, H. Hou, Y. Zhang, M. Jing, X. Jia, X. Ji, Adv. Funct. Mater. 25 (2015) 6793–6801.
[16] L.F. Shen, E. Uchaker, X.G. Zhang, G.Z. Cao, Adv. Mater. 24 (2012) 6502–6506.
[17] M.M. Rahman, J. Wang, M.F. Hassan, D. Wexler, H.K. Liu, Adv. Energy Mater. 1 (2011) 212–220.
[18] J. Liao, V. Chabot, M. Gu, C. Wang, X. Xiao, Z. Chen, Nano Energy 9 (2014) 383–391.
[19] F. Wu, X. Li, Z. Wang, H. Guo, Nanoscale 5 (2013) 6936–6943.
[20] N. Li, G.M. Zhou, F. Li, L. Wen, H.M. Cheng, Adv. Funct. Mater. 23 (2013) 5429–5435.
[21] J. Liu, K.P. Song, P.A. van Aken, J. Maier, Y. Yu, Nano Lett. 14 (2014) 2597–2603.
[22] G. Hasegawa, K. Kanamori, T. Kiyomura, H. Kurata, K. Nakanishi, T. Abe, Adv. Energy Mater. 5 (2015) 1400730.
[23] L. Yu, H.B. Wu, X.W. Lou, Adv. Mater. 25 (2013) 2296–2300.
[24] E. Kang, Y.S. Jung, G.H. Kim, J. Chun, U. Wiesner, A.C. Dillon, J.K. Kim, J. Lee, Adv. Funct. Mater. 21 (2011) 4349–4357.
[25] L. Zhao, Y.S. Hu, H. Li, Z.X. Wang, L.Q. Chen, Adv. Mater. 23 (2011) 1385–1388.
[26] C. Wang, S. Wang, Y. He, L. Tang, C. Han, C. Yang, M. Wagemaker, B. Li, Q. Yang, J. Kim, F. Kang, Chem. Mater. 27 (2015) 5647–5656.
[27] L. Shen, X. Zhang, E. Uchaker, C. Yuan, G. Cao, Adv. Energy Mater. 2 (2012) 691–698.
[28] L. Shen, B. Ding, P. Nie, G. Cao, X. Zhang, Adv. Energy Mater. 3 (2013) 1484–1489.
[29] Q. Wu, J. Xu, X. Yang, F. Lu, S. He, J. Yang, H.J. Fan, M. Wu, Adv. Energy Mater. (2014) 1401756.
[30] Y. Tang, Y. Zhang, J. Deng, D. Qi, W.R. Leow, J. Wei, S. Yin, Z. Dong, R. Yazami, Z. Chen, X. Chen, Angew. Chem. Int. Ed. 53 (2014) 13488–13492.
[31] P. Simon, Y. Gogotsi, B. Dunn, Science 343 (2014) 1210–1211.
[32] H. Lindstrom, S. Sodergren, A. Solbrand, H. Rensmo, J. Hjelm, A. Hagfeldt, S.E. Lindquist, J. Phys. Chem. B 101 (1997) 7717–7722.
[33] K. Zaghib, M. Simoneau, M. Armand, M. Gauthier, J. Power Sources 81–82 (1999) 300–305.
[34] C. Ho, I.D. Raistrick, R.A. Huggins, J. Electrochem. Soc. 127 (1980) 343–350.
[35] D. Zhang, B.N. Popov, R.E. White, J. Power Sources 76 (1998) 81–90.
[36] S. Li, J. Niu, Y.C. Zhao, K.P. So, C. Wang, C.A. Wang, J. Li, Nat. Commun. 6 (2015) 7872.
[37] H. Chiu, X. Lu, J. Zhou, L. Gu, J. Reid, R. Gauvin, K. Zaghib, G.P. Demopoulos, Adv. Energy Mater. (2016) 1601825.

Shitong Wang received his B.S. degree in Inorganic Materials Engineering from Central South University in 2012, and he is currently a Ph.D. candidate in School of Materials Science & Engineering, Tsinghua University. In 2015, he went to Massachusetts Institute of Technology (MIT) as a visiting student supervised by Prof. Ju Li. His research mainly focuses on the synthesis and properties of advanced materials for electrochemical energy storage applications.

Dr. Yong Yang received his B.S. degree and M.S. degree from Northwest University in 2009 and 2012, respectively. He pursued his Ph.D. degree in inorganic chemistry at Tsinghua University from 2012 to 2016. His research includes the synthesis, self-assembly and properties of inorganic nanocrystals for electrochemistry and energy storage.

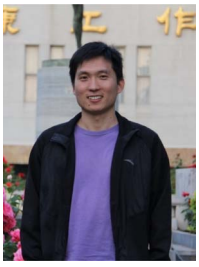

Wei Quan received his B.S. degree in Material Physics from Wuhan University of Technology in 2010, and M.S. degree in Condensed Matter Physics from Beihang University in 2013. He is currently a Ph.D. student in Material Science and Engineering, under the supervision of Prof. Zilong Tang at Tsinghua University. His research interests mainly focus on the development of novel electrochemical energy storage electrode materials.

Dr. Ye Hong received her B.S. degree in Materials Science and Engineering from South China University of Technology in 2011, and Ph.D. degree in Materials Science and Engineering from Tsinghua University in 2016 supervised by Prof. Zilong Tang. She is currently an engineer in Advanced Development & Technology Div. at Guangzhou Automobile Group Co., LTD Automotive Engineering Institute. Her research mainly focuses on the synthesis of novel electrode materials and their application in electrochemical energy storage and conversion.

Dr. Zhongtai Zhang is a professor in School of Materials Science & Engineering, Tsinghua University. He obtained his B.S. degree at Tsinghua University in 1965. He received his Ph.D. degree from The University of Tokyo in 1987. He worked as a visiting scholar (1981–1983) and a researcher (1986–1987) at The University of Tokyo, then he worked at Nagoya University as a research scientist (1992–1993). His research interests focus on luminescent materials, sensitive materials as well as materials for energy storage and environmental protection. He has over 200 publications, more than 20 granted patents and 2 monographs.

Dr. Zilong Tang is a professor in School of Materials Science & Engineering, Tsinghua University. He received his B.S. degree at Tsinghua University in 1989. He obtained his M.S. degree from Beijing Glass Research Institute in 1992 and Ph.D. degree from Tsinghua University in 1997. From 1998 to 1999, he worked as a researcher at The New Energy and Industrial Technology Development Organization (NEDO), Japan. His research interests include materials for energy storage and ceramic sensors.

Dr. Ju Li is BEA Professor of Nuclear Science and Engineering and Professor of Materials Science and Engineering at MIT. His group (http://Li.mit.edu) performs computational and experimental research on mechanical properties of materials, and energy storage and conversion. Ju obtained a Ph.D. degree in nuclear engineering from MIT in 2000, and Bachelor's degree in Physics from University of Science and Technology of China in 1994. He is a recipient of the 2005 Presidential Early Career Award for Scientists and Engineers, 2006 MRS Outstanding Young Investigator Award, and 2007 TR35 award from Technology Review magazine. Ju was elected Fellow of the American Physical Society in 2014.

Supporting Information

Ti^{3+}-free Three-Phase $Li_4Ti_5O_{12}/TiO_2$ for High-rate Lithium Ion Batteries: Capacity and Conductivity Enhancement by Phase Boundaries

Shitong Wang,[a,b] Yong Yang,[c] Wei Quan,[a] Ye Hong,[a] Zhongtai Zhang,[a] Zilong Tang [a,*] and Ju Li [b,d,*]

[a] *State Key Lab of New Ceramics and Fine Processing, School of Materials Science and Engineering, Tsinghua University, Beijing 100084, P. R. China.*

[b] *Department of Nuclear Science and Engineering, Massachusetts Institute of Technology, Cambridge, Massachusetts 02139, USA.*

[c] *Department of Chemistry, Tsinghua University, Beijing 100084, P. R. China.*

[d] *Department of Materials Science and Engineering, Massachusetts Institute of Technology, Cambridge, Massachusetts 02139, USA.*

* Correspondence to: Z.L.T. (Email: tzl@tsinghua.edu.cn) and J.L. (Email: liju@mit.edu).

This PDF file includes:

Table S1

Figures S1 to S10

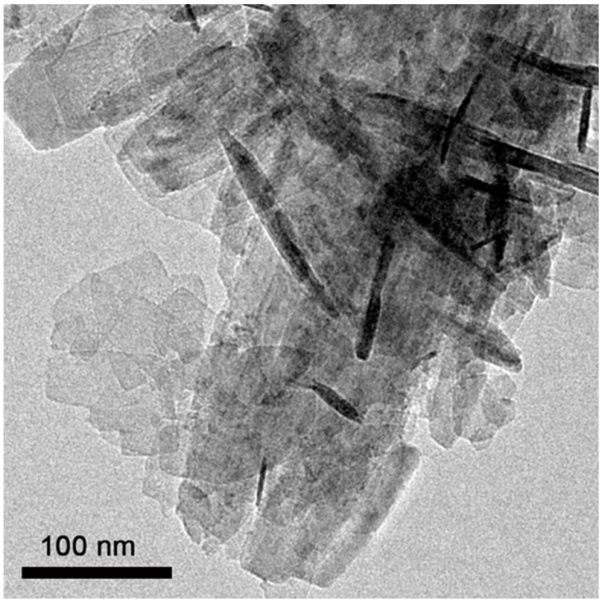

Figure S1 TEM image of LHTO/HTO precursors.

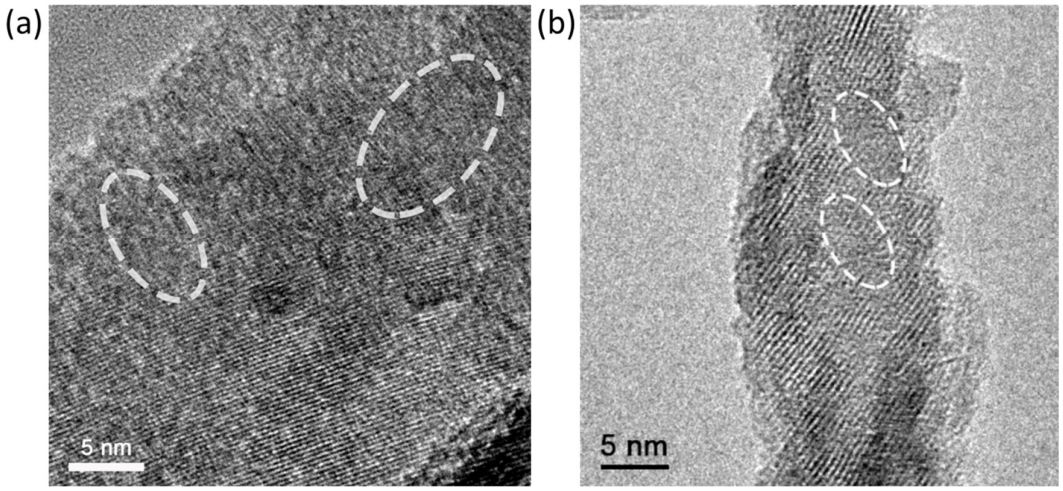

Figure S2 HRTEM images of LHTO/HTO precursors. The HTO domains with low crystallinity are illustrated in white circles.

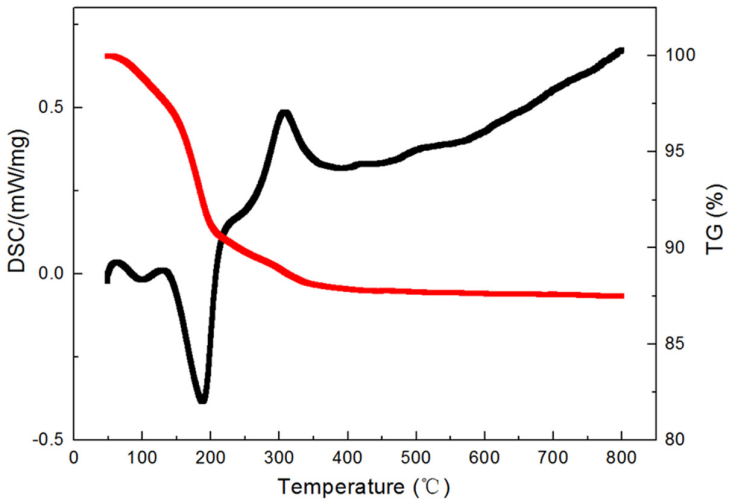

Figure S3 TG-DSC analysis of LHTO/HTO precursors.

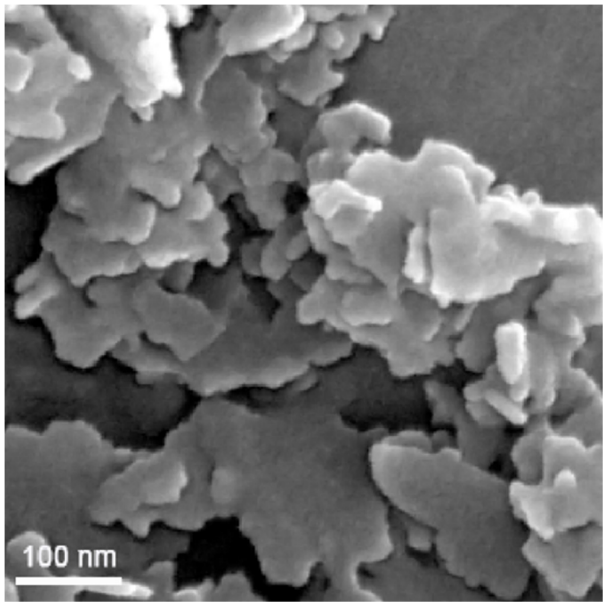

Figure S4 FESEM image of LTO/A/R.

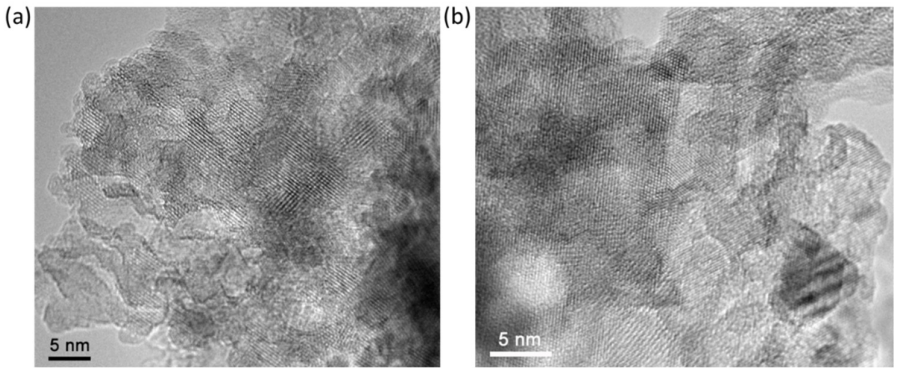

Figure S5 HRTEM images of LTO/A/R.

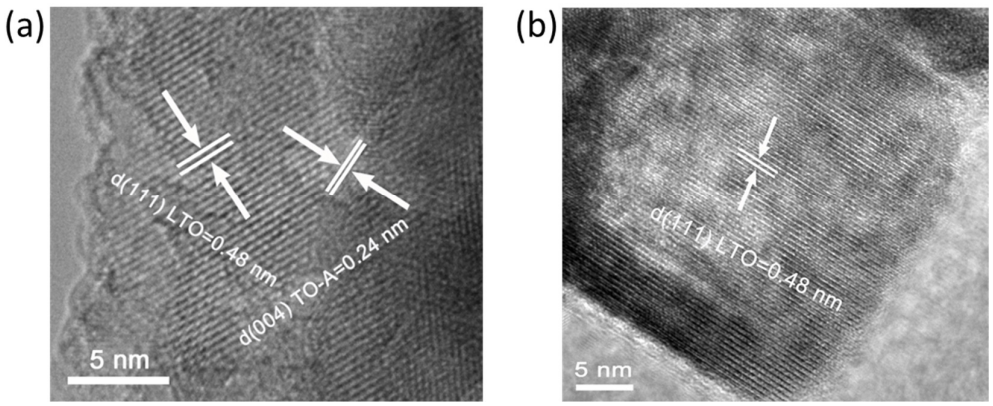

Figure S6 HRTEM images of (a) LTO/A and (b) LTO samples.

Lattice fringes of $Li_4Ti_5O_{12}$ (111) plane and TiO_2-A (004) plane can be observed in Figure S6a, which are in accordance with the result of XRD (Figure 2a). By contrast, Figure S6b demonstrates only one type of lattice fringes of $Li_4Ti_5O_{12}$ (111) plane with less phase boundaries for LTO.

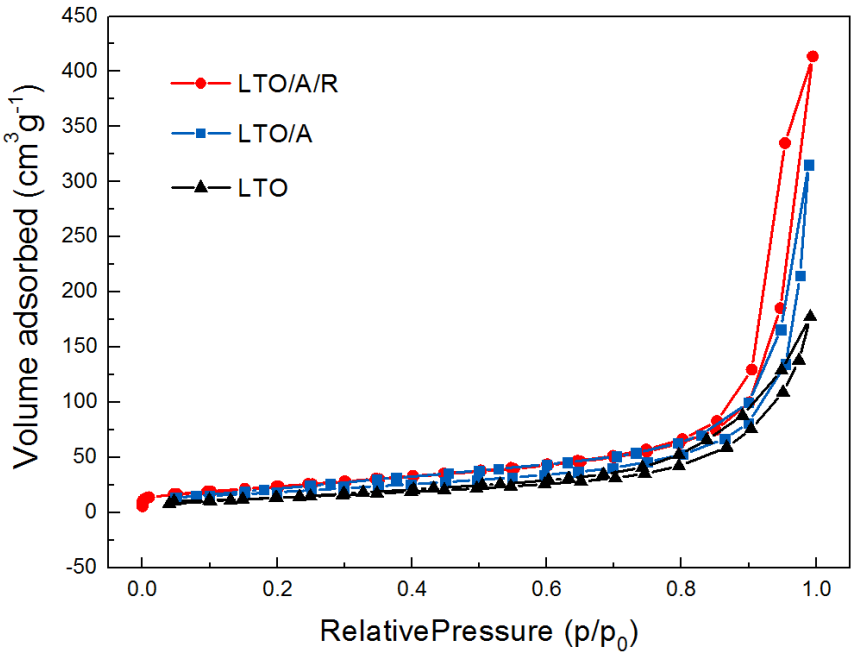

Figure S7 N_2 adsorption/desorption isotherms of LTO/A/R, LTO/A and LTO samples.

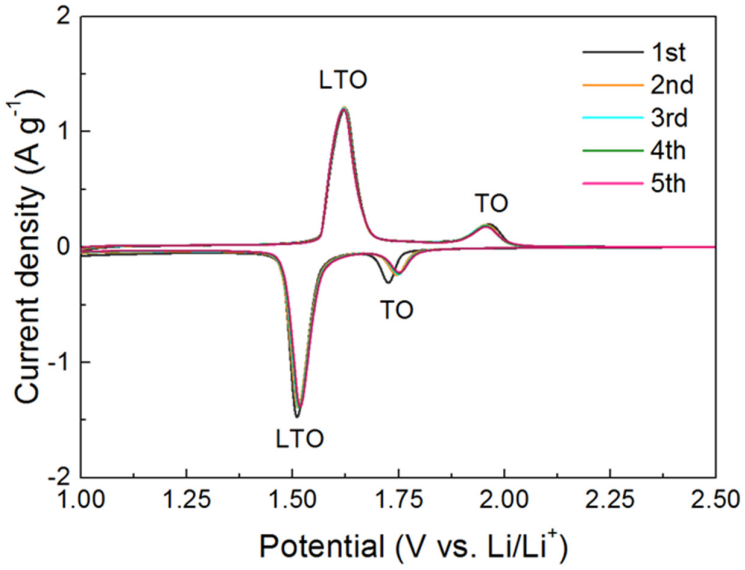

Figure S8 CV scan curves of LTO/A in the first five cycles at scanning rate of 0.1 mV s^{-1}.

Note that when CV scan curves of LTO/A/R and LTO/A varied from 0.05 to 1.6 mV s^{-1} (Figure S12a and S12b), each redox peaks became higher and broader; similarly, when the charge-discharge voltage profiles varied from 200 mA g^{-1} to 8,000 mA g^{-1} (Figure 3b and Figure S9), the voltage plateau became more slant and curved, but the features mentioned in the manuscript remain unchanged.

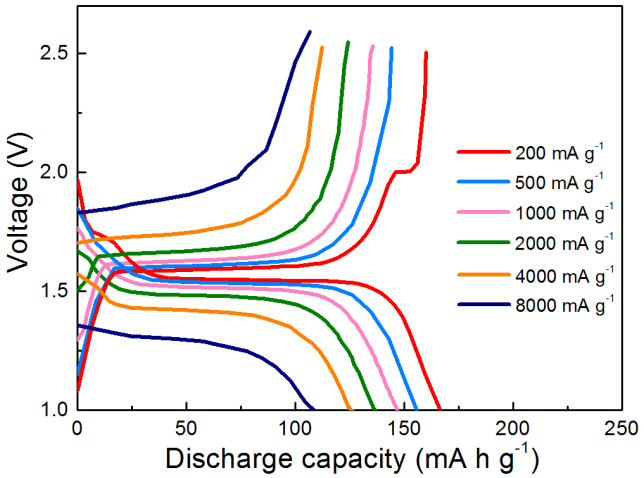

Figure S9 The charge-discharge voltage profiles of LTO/A at different current densities.

Table S1 Comparison of the rate performances of the as-prepared LTO/A/R with previously reported Ti-based anode materials. Their electrode compositions are listed using the mass ratio of active materials: conductive carbon: binder.

Materials	Electrode compositions	Loading density (mg cm^{-2})	Ref
$Li_4Ti_5O_{12}/TiO_2$ Nanoplates	80:10:10	1.0	this work
Amorphous carbon coated $Li_4Ti_5O_{12}$-anatase TiO_2	80:10:10	--	[17]
Carbon-decorated $Li_4Ti_5O_{12}$/rutile TiO_2 mesoporous microspheres	80:10:10	1-2	[9]
$Li_4Ti_5O_{12}$-anatase TiO_2 nanowire arrays	100:0:0	--	[18]
Petal-like $Li_4Ti_5O_{12}$-anatase TiO_2 nanosheets	80:10:10	1.3	[19]
$Li_4Ti_5O_{12}$ nanowires without carbon coating	100:0:0	--	[16]
$Li_4Ti_5O_{12}$ nanosheets with N-doped carbon coating	100:0:0	--	[20]
Self-supported $Li_4Ti_5O_{12}$-C nanotube arrays	100:0:0	0.42	[21]
Porous $Li_4Ti_5O_{12}$ without carbon coating	85:10:5	0.8-1.0	[22]
Mesoporous $Li_4Ti_5O_{12}$ hollow spheres without carbon coating	70:20:10	--	[23]
Mesoporous $Li_4Ti_5O_{12}$ with carbon coating	80:10:10 90:0:10	--	[24]
Porous $Li_4Ti_5O_{12}$ spheres with N-doped carbon coating	80:10:10	--	[25]
Compact $Li_4Ti_5O_{12}$ spheres with carbon coating	80:10:10	1.5	[26]
$Li_4Ti_5O_{12}$ with mesoporous carbon matrix	90:2:8	--	[27]
$Li_4Ti_5O_{12}$ micro-spheres/ carbon textiles	80:12:8	--	[28]
Anatase/ TiO_2(B) nanosheets without carbon coating	70:10:20	4-6	[29]
Gel-like TiO_2-based nanotubes	100:0:0	0.3-0.5	[30]
Ti^{3+} self-doped rutile TiO_2 nanorods	75:15:15	1.0-1.2	[15]

Note that the loading density of Ref. [29] is much higher than that of our work and other references, we then illustrate the electrochemical performances of our materials with the same loading density to make the comparison relatively fair (see Figure S10-11).

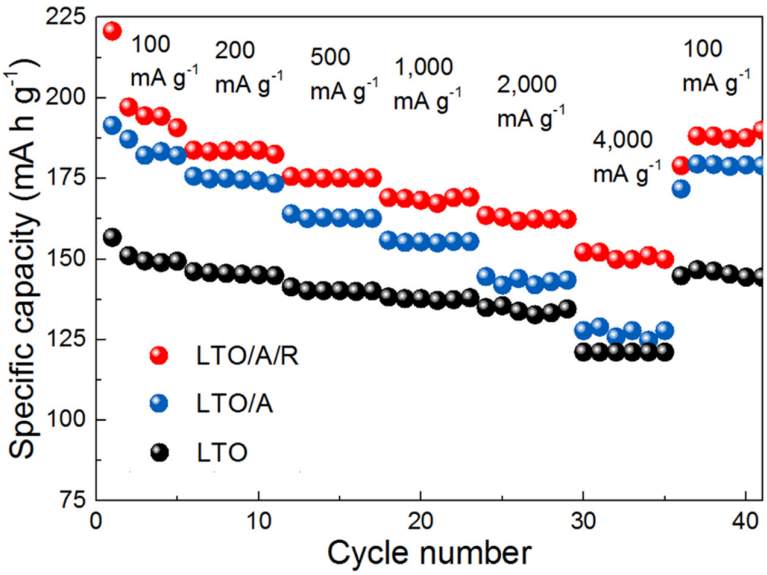

Figure S10 Rate capabilities among LTO/A/R, LTO/A and LTO samples at current densities from 100 to 4,000 mA g^{-1} with loading density of 4~5 mg cm^{-2}.

At a relative low current density (100 mA g^{-1}), the electrode delivers a stable specific capacity as high as 190 mAh g^{-1}. As the current increased from 200 to 2,000 mA g^{-1}, the specific capacities only slightly decreased from 184 to 175, 168 and 162 mA h g^{-1}, respectively. Even at very high current density of 4,000 mA g^{-1}, the specific capacities remain as high as 150 mA h g^{-1}, corresponding to 79% of that at 100 mA g^{-1}. For comparison, when the current density increases from 100 to 2,000 mA g^{-1}, the rate capabilities of LTO/A and LTO electrodes drop quickly from 183 to 142 mA g^{-1} and from 149 to 132 mA g^{-1}, respectively. At higher current density of 4,000 mA g^{-1}, the capacities of LTO/A and LTO tend to be similar, which are about 80 % of that for LTO/A/R. This phenomenon might be caused by unsatisfactory electron conductivity of LTO/A with lower crystallinity compared to LTO.

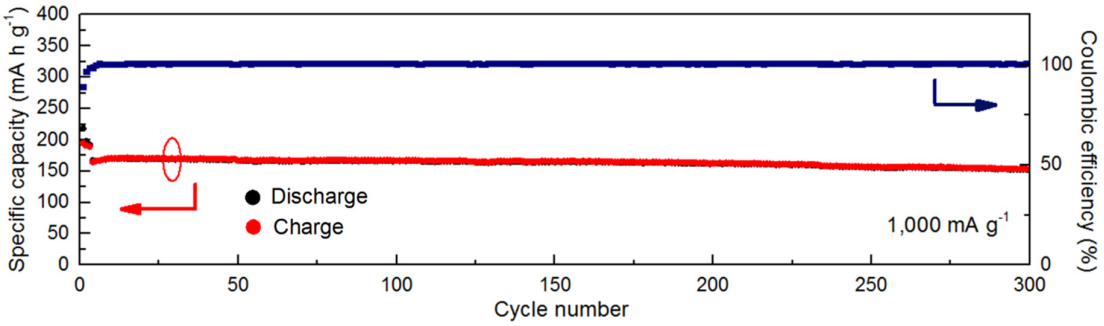

Figure S11 Graph of cycling stability and Coulombic efficiency of LTO/A/R at 1,000 mA g^{-1} with loading density of 4~5 mg cm^{-2}.

The LTO/A/R electrode exhibits superior cycling capacity of about 167 mA h g^{-1} at a high current rate of 1,000 mA g^{-1}, and capacity retention after 300 cycles is above 91%, which could prove our statement in a more persuasive way.

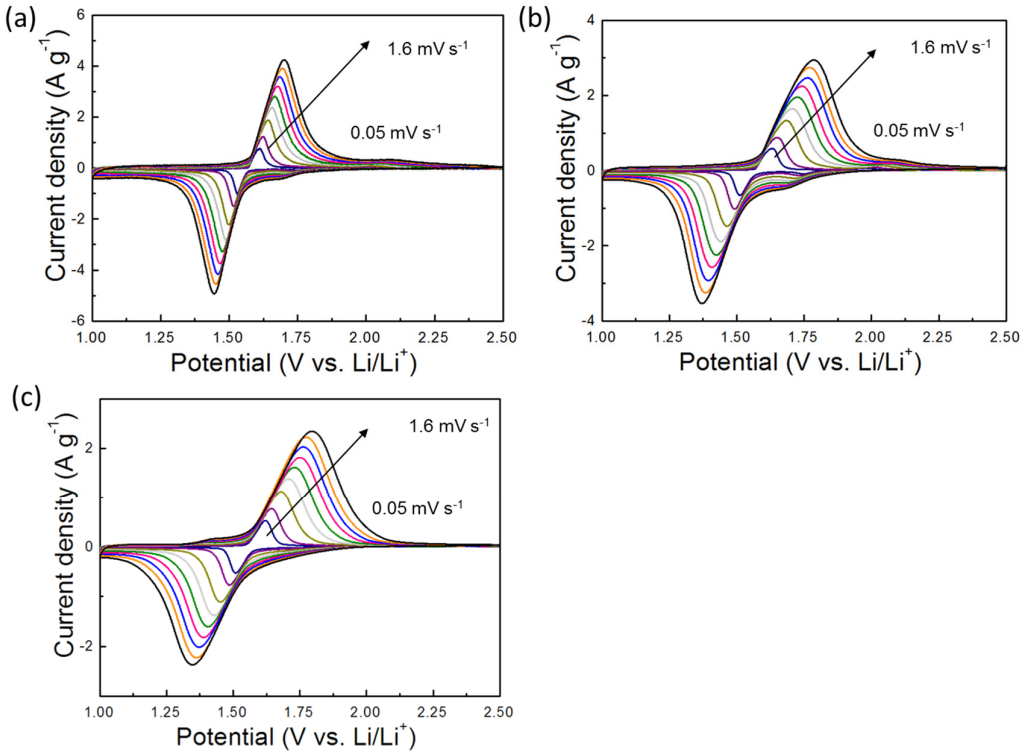

Figure S12 Cyclic voltammetry curves from 0.05 to 1.6 mV s^{-1} for comparison among (a) LTO/A/R, (b) LTO/A and (c) LTO electrodes.

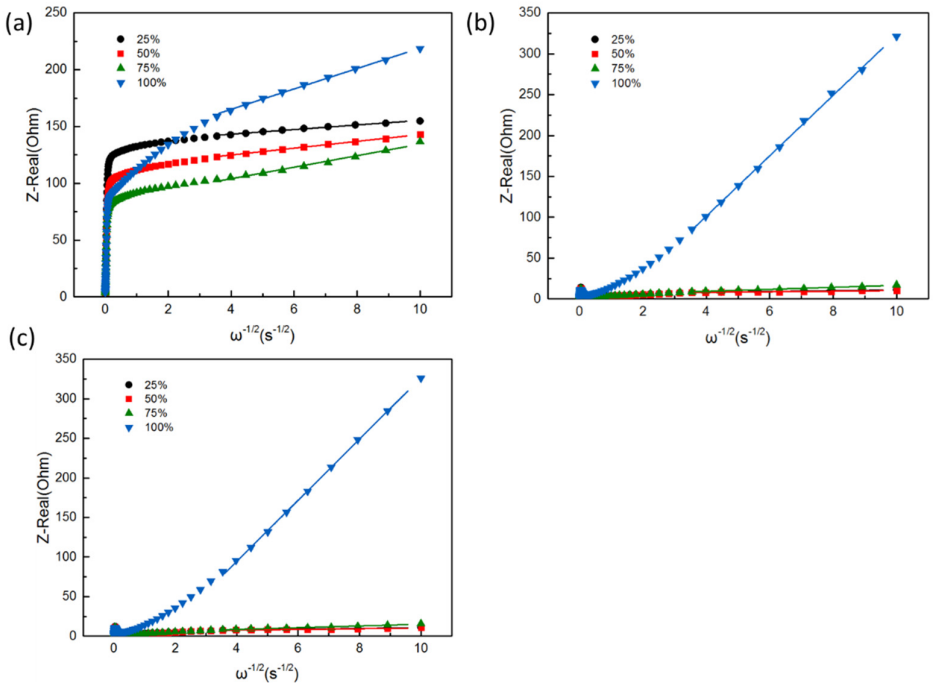

Figure S13 Z' vs. $\omega^{-1/2}$ plots in the low frequency region obtained from EIS measurements of (a) LTO/A/R, (b) LTO/A and (c) LTO electrodes.

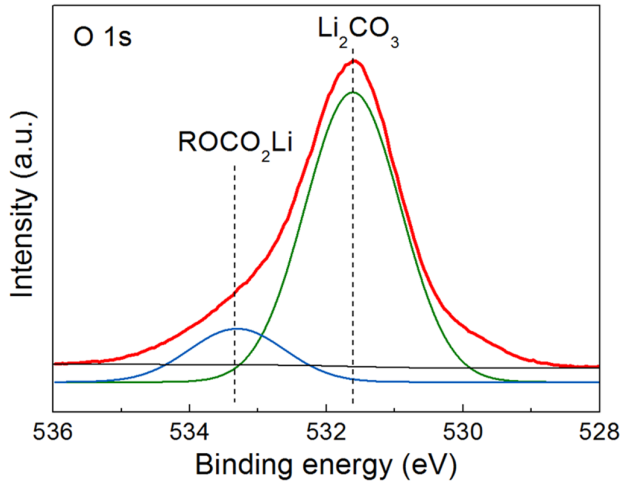

Figure S14 O 1s XPS spectra of LTO/A/R after 4,000 cycles. Red: observed data; black: background; blue and green: fitting data.

The possible SEI formation mechanisms are as follows: i) hydrolytic decomposition of electrolyte because of trace amounts of water: the formation of a SEI like layer in the first cycle might be caused by the processes such as proton recombination [S1]. ii) intrinsic catalysis by Ti^{4+} species: during the discharge process, Ti^{3+} is oxidized to Ti^{4+}, whereby the latter species may

have a catalytic influence on the electrolyte decomposition. Passivating the surface would effectively rule out the influence of this reaction [S2]. iii) electrolyte reduction from lithiated LTO: The formation of both inorganic Li_2CO_3 and organic $(CH_2CH_2OLi)_2$ is mainly triggered from the reduction of EC [S3, S4].

References

[S1] M. He, E. Castel, A. Laumann, G. Nuspl, P. Novak, E. J. Berg, J. Electrochem. Soc. 162 (2015) A870-A876.

[S2] Y. He, B. Li, M. Liu, C. Zhang, W. Lv, C. Yang, J. Li, H. Du, B. Zhang, Q. Yang, J. Kim, F. Kang, Sci. Rep.-UK 2 (2012) 913.

[S3] R. Imhof, J. Electrochem. Soc. 145 (1998) 1081.

[S4] K. Xu, Chem. Rev. 104 (2004) 4303-4418.